Calcium oscillations in wounded fibroblast monolayers are spatially regulated through substrate mechanics

Josephine Lembong[1]*, Benedikt Sabass[2,3]*, and Howard A. Stone[2]

[1] Department of Chemical and Biological Engineering, Princeton University, Princeton, NJ 08544, USA (*Current address*: Department of Bioengineering, University of Maryland, College Park, MD 20742, USA)

[2] Department of Mechanical and Aerospace Engineering, Princeton University, Princeton, NJ 08544, USA

[3] Institute of Complex Systems -2, Forschungszentrum Jülich, D-52425 Jülich, Germany

** These authors contributed equally to this work*

Corresponding authors: Benedikt.Sabass@bioquant.uni-heidelberg.de, hastone@princeton.edu

SUPPLEMENTARY MATERIAL

MOVIE CAPTIONS

Movie S1. A fibroblast cell monolayer on PA gel (E = 360 Pa) exposed to a wound edge.

Movie S2. A fibroblast cell monolayer on PA gel (E = 8300 Pa) exposed to a wound edge.

Movie S3. A fibroblast cell monolayer on glass ($E = \sim O(10\ \text{GPa})$) exposed to a wound edge.

.

SUPPLEMENTARY MATERIALS AND METHODS

Correlation of Ca^{2+} dynamics and cell migration in the context of migrating cell ensembles.

Table S1. Selected studies showing the correlation of Ca^{2+} dynamics and cell migration on cell ensembles.

Study	Experimental system	Main findings
Gomez et al., 1995 [38]	Neuronal growth cones on glass	Growth cone migration rate is reduced by intracellular Ca^{2+} spikes.
Robles et al., 2003 [39]	Xenopus neuronal growth cones on glass	Ca^{2+} signals suppress axon outgrowth and reduce filopodial motility through calpain-dependent regulation of signaling at integrin-mediated adhesion sites.
Komuro & Rakic, 1996 [40]	Cerebellar granule cells on glass	Amplitude and frequency of intracellular Ca^{2+} fluctuations are correlated positively with neuron migration speed.
Mandeville et al., 1995 [41]	Human neutrophils on glass	Levels of intracellular Ca^{2+} correlate with migration speed and persistent forward motion.
Tsai et al., 2014 [42]	Human umbilical vein endothelial cells (HUVECs) on glass	Leader cells near the colony edge have larger internal gradients of Ca^{2+} pumping rate and second messenger IP3 to promote directed cell migration.

Characterization of PA gels

Elastic properties of the PA gels were measured by a stress-controlled rheometer (Anton Paar, Physica MCR 301). Most of the rheometry experiments were carried out at 23°C by using a cone-plate geometry to obtain a homogeneous velocity gradient throughout the sample (Measuring cone CP50-1/TG). For the higher elastic moduli, the data was confirmed by using a rough parallel-plate setup (Plate PP50/S). The rough plate prevents slippage between the sample and the instrument. In the parallel-plate mode, the gap thickness was chosen to be 0.5 mm. After preparing the gel and adding the polymerization initiator, the liquid was placed on the rheometer and the measurement plate was moved into measurement position. After letting the gel polymerize between the plates for 15 min., the rim of the plates was covered with a small film of water to avoid evaporation. Polymerization was allowed to proceed for 45-60 min. before data recording and it was checked that the polymerization proceeded long enough to make sure that elastic properties did not change anymore. Gelation of the substrate produces significant normal forces on the rheometer plate, which can affect the measurement of shear moduli. Therefore, the normal forces were set to zero by slight adjustment of the gap size before commencing the final measurement. For the employed PA gels, we obtained the shear moduli given in table S2. Assuming a Poisson ratio of $s = 0.47$ (1), the Young's modulus was calculated as $E = 2\ (1 + s)\ G'$. At typical oscillation frequencies of 0.01-10 Hz, the loss modulus was found to be 1-2 orders of magnitude smaller than the shear modulus.

Table S2. Elastic properties of polyacrylamide gels used in wounded cell monolayer experiments.

Gel type	% Acrylamide	% Bis-Acrylamide	Shear modulus (Pa)	Std dev of sample (Pa)	Loss modulus (Pa)	Std dev of sample (Pa)	Estimated Young's modulus (Pa)
1	3	0.06	120	43	6	5	360
2	3	0.1	230	25	6	4	690
3	5	0.035	650	37	18	8	1900
4	5	0.05	950	140	16	8	2800
5	7.5	0.05	2800	320	42	37	8300
6	10.52	0.14	8400	1300	10	11	25000

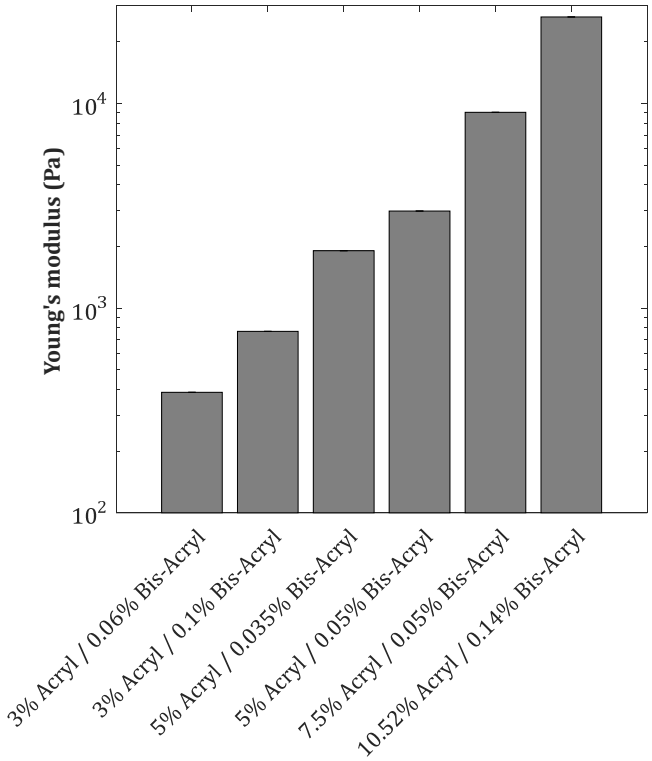

Figure S1. Elastic properties of PA gels used in wounded cell monolayer experiments, as measured by rheometry.

Traction Force Microscopy (TFM) for determination of cellular forces

Live cell traction force measurements were performed on a Leica SP5 confocal microscope using a HeNe laser at 543 nm. The PA gel substrates were prepared as described in the methods section of the main text and contain carboxylate-modified, orange fluorescent beads with a diameter of 200 nm.

The TFM data was acquired by capturing images of the beads every 5 minutes in an image plane immediately below the cells. Cells were then detached from the PA substrate by perfusing trypsin solution into the imaging chamber, thus allowing the substrate to relax from its cell-induced strained state. Following cell removal, *z*-stacks of the unstrained PA substrate were acquired with 200 nm vertical increments. For each frame in the TFM image sequence, a reference image was selected from the unstrained *z*-stack by maximizing the correlation coefficient between the TFM images and laterally shifted images from the *z*-stack. Substrate deformations between the stressed state with cells and the unstressed reference state were measured using correlation-based tracking of the fluorescent beads (2). Due to the large field of view and long imaging periods, images from the reference state were usually not only shifted, but also rotated with respect to the original image. We removed these perturbations on the level of the displacement field. First, we subtracted the mean of the two components of the deformation field, thus positioning the center of rotation in the center of the image. Second, the average rotation angle $\langle\alpha\rangle$ was calculated using Stokes theorem. Finally, rotation was removed by subtracting from each displacement u a vector u' corresponding to the average rotation angle of the whole image.

The calculation of tractions from the displacement field was done in Fourier space. The wave vector in the horizontal plane is denoted by k_i, where $i \in \{1,2\}$ and the norm of the wave vectors is written as $k = \sqrt{k_1^2 + k_2^2}$. The Fourier-transformed displacement is denoted by $\tilde{u}_i$ and the traction acting in the *x*-*y* plane is denoted by $\tilde{t}_i$. Traction and displacement are related in Fourier space through multiplication by a Green's

function as $\tilde{u}_i = \sum_j \tilde{G}_{ij}\tilde{t}_j$. The Green's function relating traction to displacement on a substrate with thickness *h* reads (3, 4):

$$\tilde{G}_{ij}(k_1,k_2,h) = \frac{2(1+s)}{E\ k^3}\left(\tanh(kh)k^2\delta_{ij} + k_i k_j \frac{\left(1-s-g\tanh(kh)\right)}{g} \right),$$

where $g = \left((3-4s)\cosh(kh)^2 + (1-2s)^2 + (kh)^2\right) \Big/ \left((3-4s)\sinh(kh)\cos(kh) + kh\right)$.

The traction was calculated from the Fourier-transformed displacement field via (2):

$$\tilde{t}_i = \sum_{l,j}\left(\sum_m \tilde{G}_{ml}\tilde{G}_{mi} + \lambda^2\delta_{il} \right)^{-1} \tilde{G}_{jl}\tilde{u}_j ,$$

where λ^2 is a regularization parameter. The regularization parameter is to be chosen to be as small as possible, but large enough to suppress spurious noise in the image. Here, we chose to scale out the substrate-dependence as $\lambda = \lambda'(2+2s)/E$, and fixed $\lambda' = 10$ for all substrate properties. For our data, using a Green's function with *h* = 100 μm produced similar results as using the assumption that *h* approaches infinity. Edge effects resulting from the analysis in Fourier space were suppressed by zero-patterning the data.

Since the field of view in this experiment does not cover the whole monolayer, forces do not exactly balance each other. Consequently, the Fourier coefficient corresponding to a spatially constant traction component does not vanish. In our experiment, we roughly estimated the constant traction component from the condition that the traction outside the edge must vanish approximately.

Monolayer traction forces on different substrates

To compare the traction on different cell substrates, we align the *x*-axis of a cartesian coordinate system with the edge of the monolayer such that the *y*-axis points towards the cells. The reconstructed traction is then averaged over the *x*-component, yielding a magnitude $T(y) = \frac{1}{L_x}\int_0^{L_x}\left[{t_x}^2(x,y) + {t_y}^2(x,y) \right]^{1/2} dx$ and mean traction components $\left\langle t_i(y) \right\rangle = \frac{1}{L_x}\int_0^{L_x} t_i(x,y)dx$. The quantities $T(y)$ and $\left\langle t_i(y) \right\rangle$ are subsequently averaged over all experiments.

For each measured cell monolayer, we employ two TFM data sets taken ~60 min. apart from each other, to ensure that short-lived temporal traction features do not dominate our results. Increasing the Young's modulus *E* of the substrate from 690 Pa to 8300 Pa, we observe that the traction magnitude $T(y)$ has a local maximum at the edge of the monolayer only on the softer substrates (figure S2(a(i), b(i), c(i))). The average traction *x*-component that is approximately parallel to the edge $\left\langle t_x(y) \right\rangle$ generally has a small value and fluctuates for all conditions around zero (figure S2(a(ii), b(ii), c(ii))). The average traction in the *y*-direction $\left\langle t_y(y) \right\rangle$ has a maximum close to the edge for all conditions. However, for *E* = 2800Pa and *E* = 8300 Pa, we also observe strong traction in the monolayer far behind the edge (figure S2(a(iii), b(iii), c(iii))). Note that the maximum of $\left\langle t_y(y) \right\rangle$ close to the edge does not imply a maximum of $T(y)$ for the datasets on *E* = 8300 Pa. Positive and negative traction on one line of constant *y* compensate each other in $\left\langle t_y(y) \right\rangle$ but increase the magnitude $T(y)$.

Stresses acting between neighboring cells cause a local imbalance of traction. Thus, the integral of traction is a measure for the stress inside the cell monolayer. To obtain an estimate for the stress along the *y*-coordinate, we calculate the integral $\int_{y_0}^{y} \langle t_y(y') \rangle dy'$ for the three investigated substrate rigidities (figure S2(d)). Because of the uncertainties associated with our measurement, this estimate is very crude. Qualitatively, we observe that the monolayer stress that acts normal to the edge increases on stiff substrates with distance from the edge.

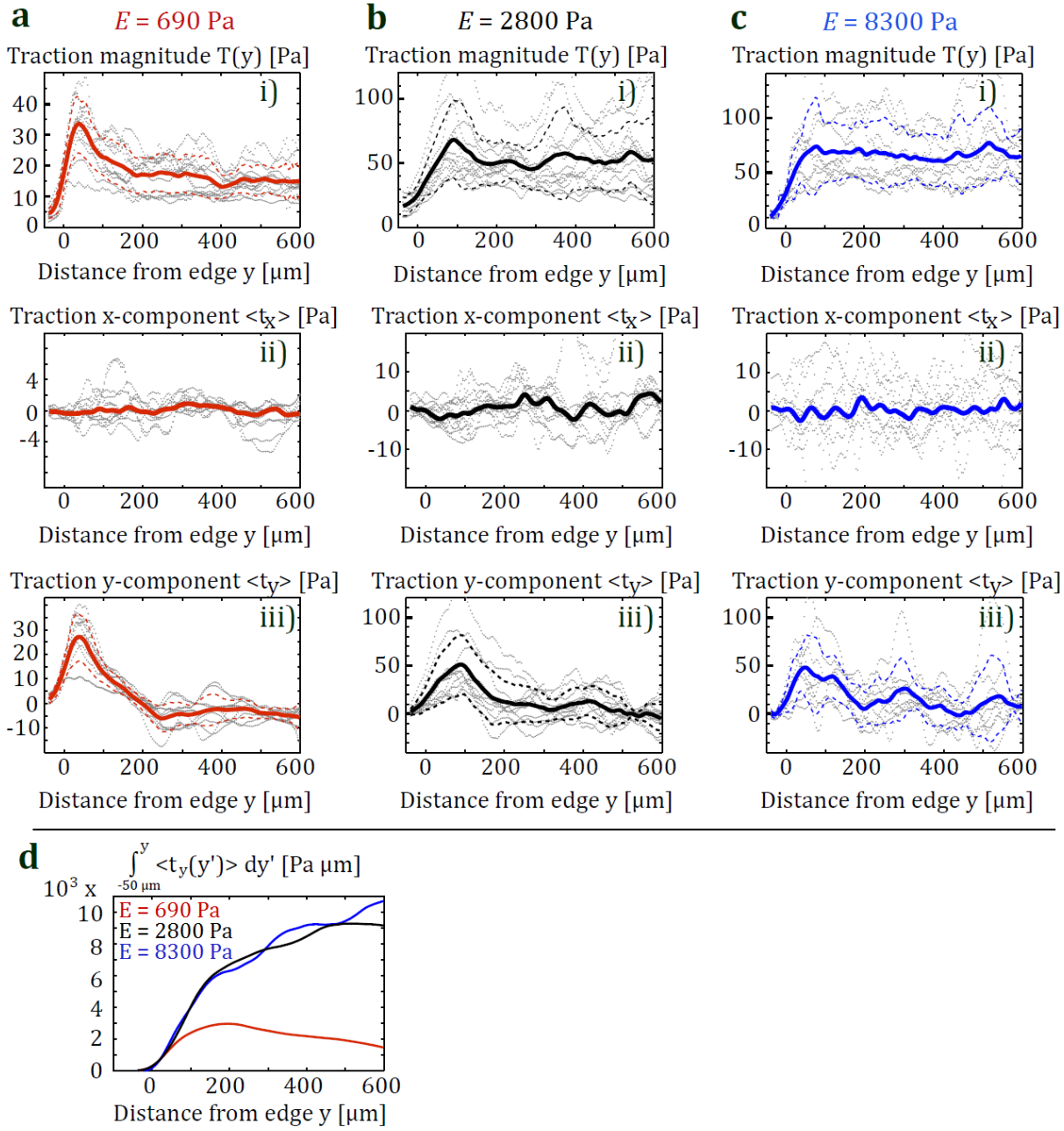

Figure S2. Monolayer traction forces on various PA substrates. (a-c) Traction magnitude ($T(y)$), average traction *x*-component parallel to the edge ($\langle t_x \rangle$), and average traction in *y*-direction, ($\langle t_y \rangle$) for E = 690 Pa (a), E = 2800 Pa (b), and E = 8300 Pa (c). (d) Estimated *y*-component of stress inside the monolayer.

Effect of cell monolayer density on the number of cells exhibiting calcium oscillations

Following the creation of a wound edge in fibroblast monolayers on 2D PA and glass substrates, cells display oscillatory Ca^{2+} behavior. More cells exhibit Ca^{2+} oscillations in denser monolayers, indicating that wound-induced Ca^{2+} oscillations are a collective phenomenon.

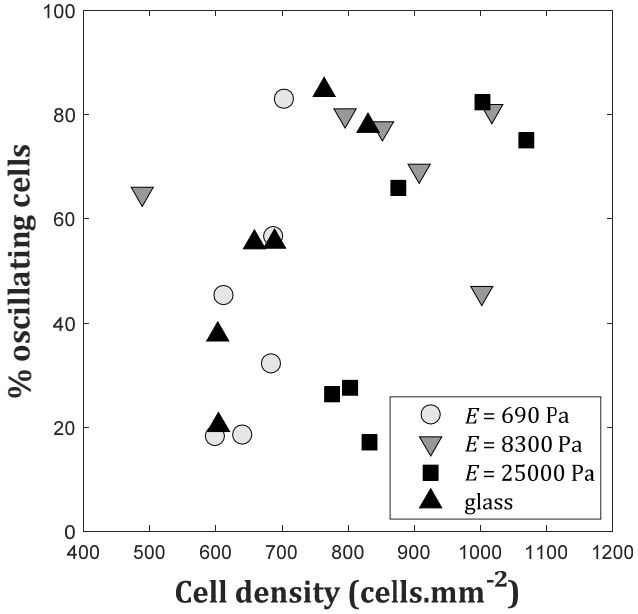

Figure S3. Percentage of cells exhibiting wound-induced Ca^{2+} oscillations increases with cell density.

Analysis of interspike time of calcium oscillations for various substrates

The time intervals between calcium peaks shown vary considerably, which may be attributed to variations on the level of individual cells. However, the scatter of oscillation periods can also be caused by variability among different cells. To test how cell-cell variations cause spread of the oscillation period, we follow Skupin et al. and Thurley et al. (5, 6) and calculate the average oscillation period together with the variance of the oscillation period for individual cells (figure S4(a-b)). As shown earlier for other types of cells (6), we find a linear correlation between the average oscillation period and the standard deviation (std) of the oscillation periods for fibroblasts. Thus, variability of oscillations on the single cell level is proportional to the period of oscillations.

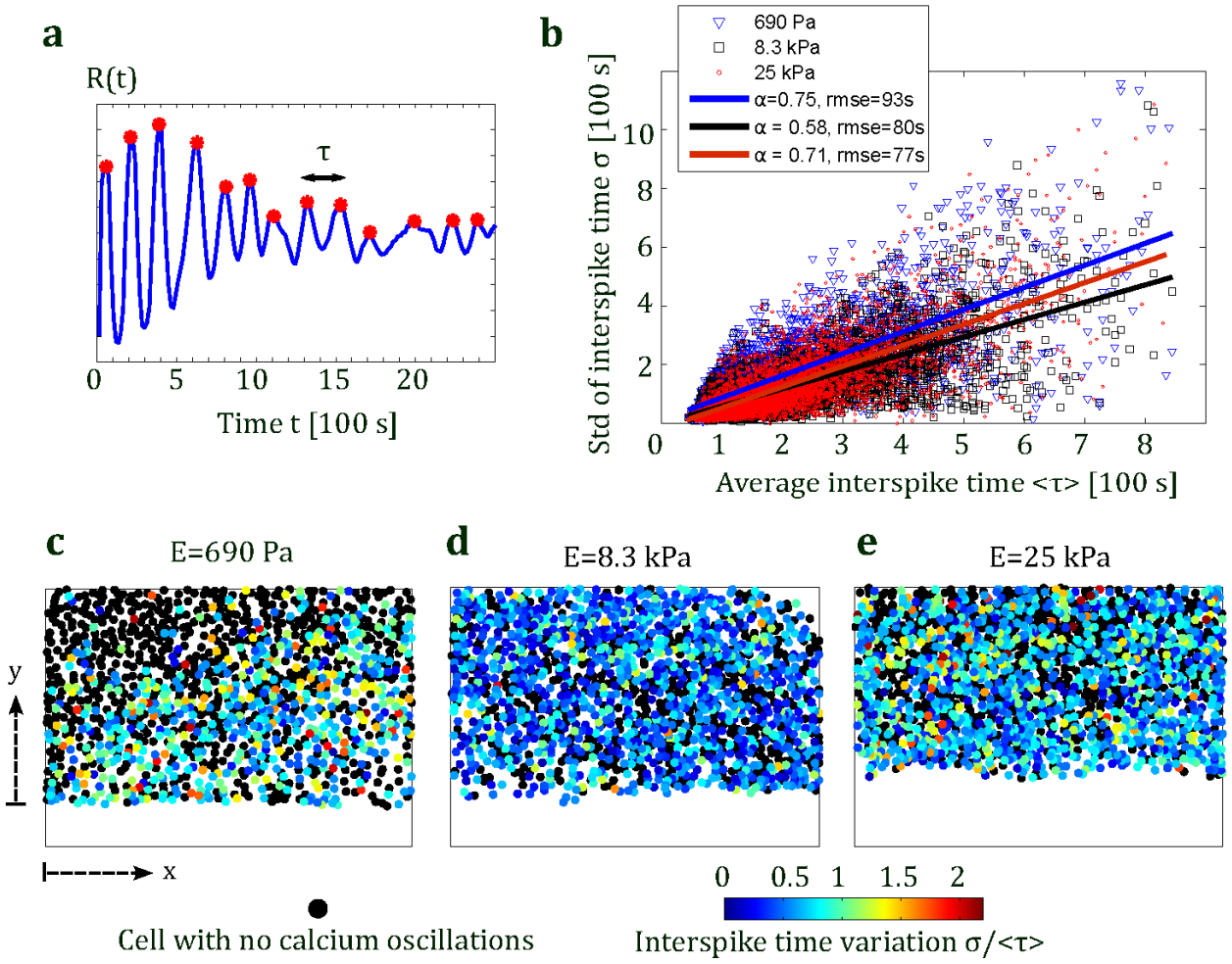

Figure S4. (a) Normalized fluorescence intensity $R(t)$ of one cell over time. The interval between individual spikes is denoted by τ. The average of the interspike time <τ> is calculated for individual cells from recordings of 45 minutes. (b) Average time between spikes <τ> vs. standard deviation σ of time between spikes for individual cells. Note that σ correlates well with <τ>. A fit of the linear relationship σ = α <τ> + const. leads to slopes α that are smaller than unity. We find that the time between spikes does not follow a Poisson distribution. We also find that the slopes α depend significantly on the substrate rigidity ($p < 0.01$). However, the dependence of α on substrate rigidity does not appear to follow a clear trend (n=4 for each condition). (c-e) Spatial localization of the relative variability of the calcium oscillations σ/<τ>. The variability σ/<τ> is not enhanced in particular spatial regions in the sheet. However, on the soft substrate with E = 690 Pa, cells oscillate more when they are close to the edge.

Spatial distribution of calcium oscillation period in wounded fibroblast monolayers

The calcium oscillation period is not significantly affected by the distance from the wound edge on our PA gels with Young's modulus E = 690 Pa, E = 8300 Pa, and E = 25000 Pa (figure S5).

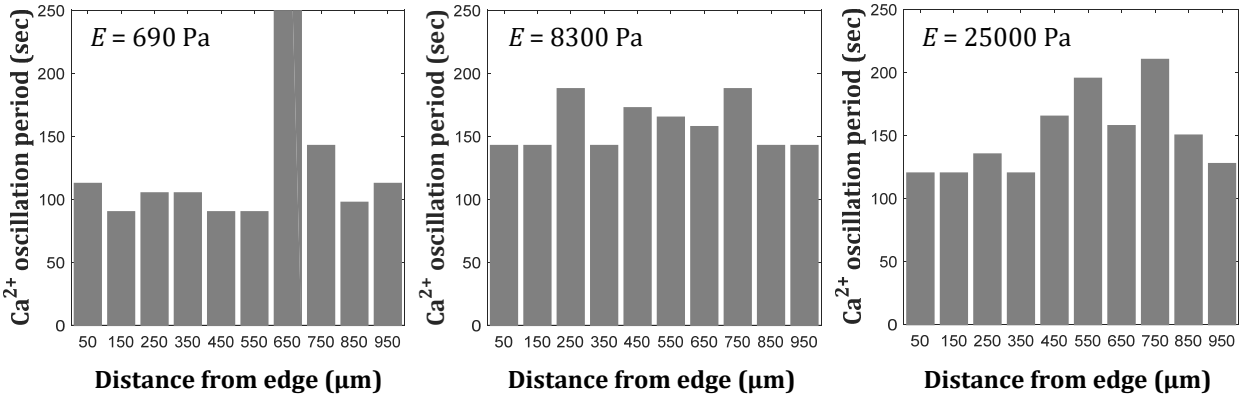

Figure S5. Spatial distribution of Ca^{2+} oscillation period in wounded fibroblast monolayers on PA gel, E = 690 Pa, E = 8300 Pa, and E = 25000 Pa.

Non-monotonic dependence of oscillation period on substrate stiffness

Fibroblast cell monolayers on 2D PA substrates and on glass exhibit Ca^{2+} oscillations upon the creation of our wound system. The dominant oscillation period for fibroblast cells in such monolayers show no general trend of dependence on the substrate's Young's modulus.

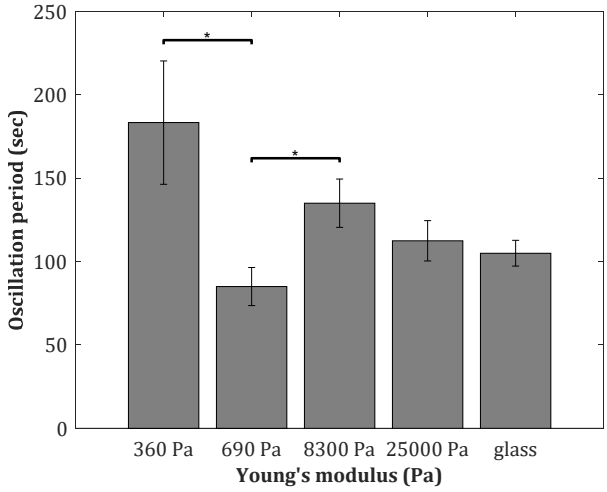

Figure S6. Wound-induced calcium oscillation period as a function of the substrate elasticity. Values are the averages of six experiments and error bars are standard errors of the mean (*$p \leq 0.05$).

Effect of myosin-based contractility on wound-induced Ca^{2+} oscillations behavior

Blebbistatin treatment to fibroblast cell monolayers causes a decrease of the fraction of the cells that exhibits wound-induced Ca^{2+} oscillations.

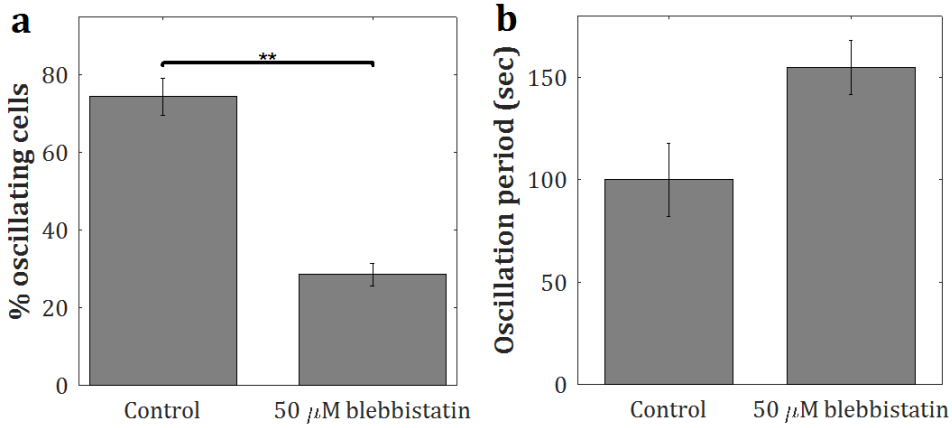

Figure S7. Effect of blebbistatin on wound-induced Ca^{2+} oscillations on PA gel, E = 25000 Pa. Values are the averages of three experiments and error bars are standard errors of the mean (**$p \leq 0.01$).

Cell area in a wounded fibroblast monolayer is independent of substrate stiffness

While it is known that substrate stiffness changes the cell spreading area for individual cells, it has also been reported that cell monolayers react less strongly to substrate rigidity (4, 7). Accordingly, we observe no strong and consistent difference in spreading area of our wounded 3T3 monolayers on substrates with varying rigidity. Area covered by cells in these systems were quantified using FIJI (8).

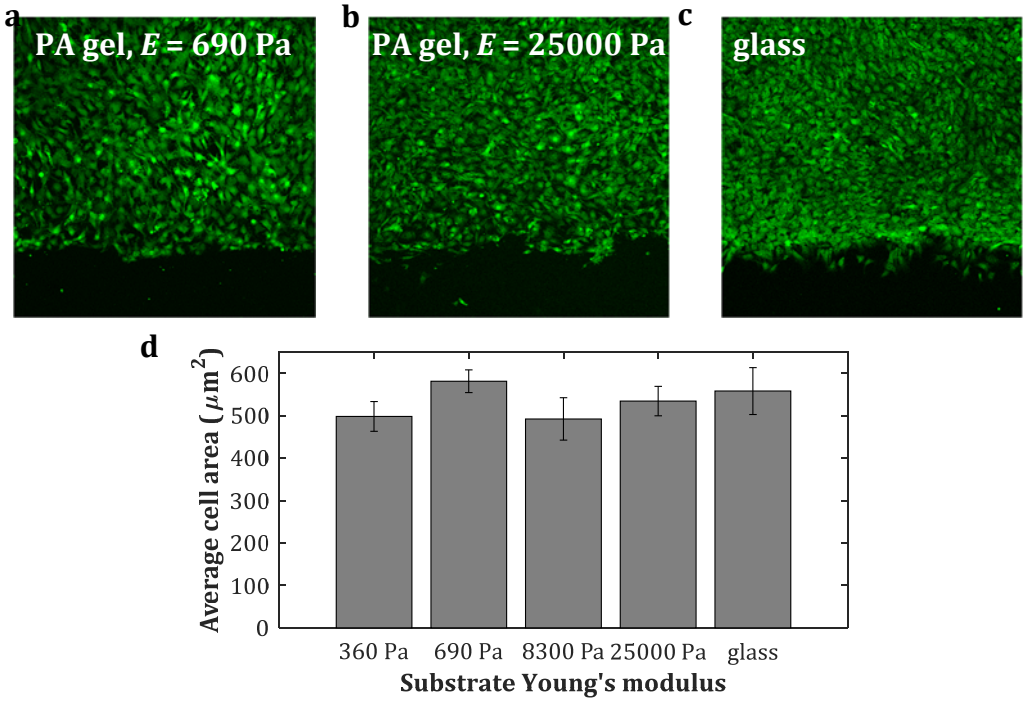

Figure S8. Cell area is independent of substrate stiffness in 3T3 monolayers. (a-c) Wounded 3T3 monolayers on various substrates (a) PA gel, E = 690 Pa, (b) PA gel, E = 25000 Pa, and (c) glass. (d) Average cell area as a function of Young's modulus. Values are averages of six samples and error bars are standard errors of the mean.

The distance from the wound edge with most oscillating cells increases with substrate stiffness

We define oscillating cells as those having at least two calcium peaks and plot the distance from the wound edge with maximum number of oscillating cells for the various substrate stiffnesses (figure S9). The average distance from the wound edge with most oscillating cells increases with substrate stiffness. Although the trend is weak, it agrees with the results shown in figure 4(d) where for softer substrates the highest number of Ca^{2+} oscillations are seen closer to the edge. For stiff substrates (25 kPa and glass), the distance with most oscillating cells is roughly the same as the distance with most Ca^{2+} oscillations, around 0.5-0.6 mm (figure 4(d)), while for the softer substrates, the distance with most oscillating cells is greater than distance with most Ca^{2+} oscillations.

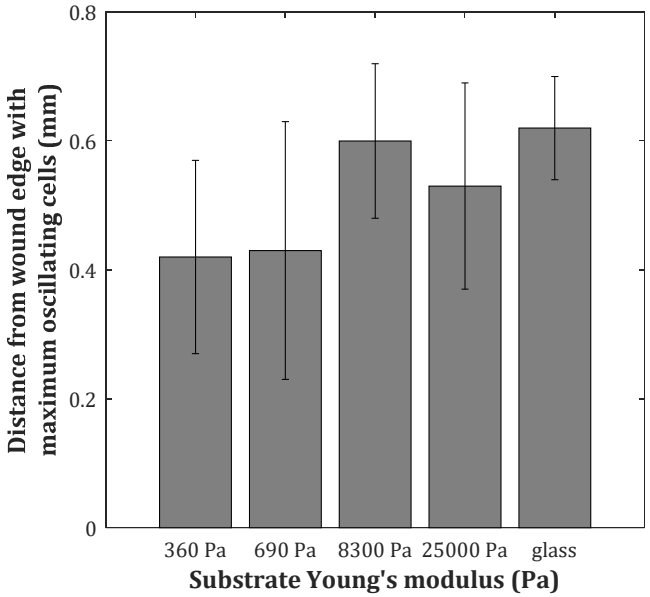

Figure S9. The average distance of maximum oscillating cells increases with substrate stiffness.

Correlation of calcium responses in wounded fibroblast monolayers on PA substrates

To understand the interactions between cells' calcium responses in a wounded monolayer, we calculate the rate of change of calcium intensity $\dot{R}(t)$ and then define the pair cross-correlation function $C(\tau)_{ij}$ for all pairs of nearest neighbors (i,j) in the monolayer (9):

$$\dot{R}_i(t) = \frac{dR_i(t)}{dt} - \left\langle \frac{dR_i(t)}{dt} \right\rangle$$

$$C(\tau)_{ij} = \frac{1}{\sqrt{\sigma_i \sigma_j}} \left\langle \dot{R}_i(t) \dot{R}_j(t+\tau) \right\rangle$$

where $\langle dR_i(t)/dt \rangle$ represents the time-averaged value, and σ_i is the variance of $\dot{R}_i(t)$. The cross-correlation function $C(\tau)_{ij}$ is then averaged over all the nearest-neighbor pairs i,j for PA gels, E = 690 Pa and 8300 Pa.

On PA gels with Young's modulus of 690 Pa and 8300 Pa, Ca^{2+} responses of nearest neighbor cells in wounded fibroblast monolayers reveal synchronization events as indicated by the positive correlation peak at $\tau = 0$, which is consistent with the short-range gap junctional Ca^{2+} communication observed in similar fibroblast systems (9, 10).

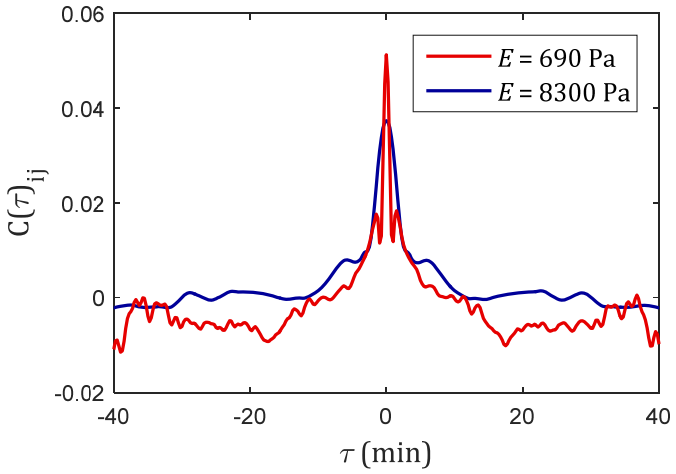

Figure S10. Cross-correlation analysis for Ca^{2+} response in wounded fibroblast monolayers on PA gel, E = 690 Pa and E = 8300 Pa.

Uniformity of cell density with distance from the wound edge

Cell density is observed to be uniform throughout the various distances from the wound edge on our experiments on both soft (E = 690 Pa) and stiff PA gels (E = 8300 Pa) (figure S11). The observed localization of traction forces during wound-induced Ca^{2+} responses on these gels (figure 5, figure S2) are therefore not caused by the cell density localization.

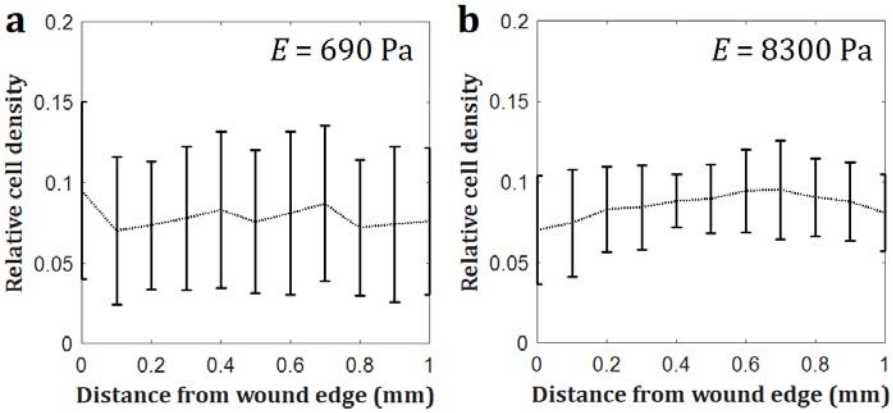

Figure S11. Uniformity of cell density with distance from the wound edge for cells on PA gel: (a) E = 690 Pa, (b) E = 8300 Pa.

SUPPLEMENTARY REFERENCES

1. Boudou T, Ohayon J, Picart C, Tracqui P. An extended relationship for the characterization of Young's modulus and Poisson's ratio of tunable polyacrylamide gels. Biorheology. 2006;43(6):721-8.
2. Sabass B, Gardel ML, Waterman CM, Schwarz US. High resolution traction force microscopy based on experimental and computational advances. Biophys J. 2008 Jan 1;94(1):207-20.
3. del Alamo JC, Meili R, Alonso-Latorre B, Rodriguez-Rodriguez J, Aliseda A, Firtel RA, et al. Spatio-temporal analysis of eukaryotic cell motility by improved force cytometry. P Natl Acad Sci USA. 2007 Aug 14;104(33):13343-8.
4. Trepat X, Wasserman MR, Angelini TE, Millet E, Weitz DA, Butler JP, et al. Physical forces during collective cell migration. Nat Phys. 2009 Jun;5(6):426-30.
5. Skupin A, Kettenmann H, Winkler U, Wartenberg M, Sauer H, Tovey SC, et al. How does intracellular Ca2+ oscillate: By chance or by the clock? Biophys J. 2008 Mar 15;94(6):2404-11.
6. Thurley K, Tovey SC, Moenke G, Prince VL, Meena A, Thomas AP, et al. Reliable Encoding of Stimulus Intensities Within Random Sequences of Intracellular Ca2+ Spikes. Sci Signal. 2014 Jun 24;7(331).
7. Yeung T, Georges PC, Flanagan LA, Marg B, Ortiz M, Funaki M, et al. Effects of substrate stiffness on cell morphology, cytoskeletal structure, and adhesion. Cell Motil Cytoskeleton. 2005 Jan;60(1):24-34.
8. Schindelin J, Arganda-Carreras I, Frise E, Kaynig V, Longair M, Pietzsch T, et al. Fiji: an open-source platform for biological-image analysis. Nat Methods. 2012 Jun 28;9(7):676-82.
9. Sun B, Lembong J, Normand V, Rogers M, Stone HA. Spatial-temporal dynamics of collective chemosensing. Proc Natl Acad Sci U S A. 2012 May 15;109(20):7753-8.
10. Lembong J, Sabass B, Sun B, Rogers ME, Stone HA. Mechanics regulates ATP-stimulated collective calcium response in fibroblast cells. J R Soc Interface. 2015 Jul 6;12(108).